

# Journal of Materials Chemistry A

Accepted Manuscript



This is an *Accepted Manuscript*, which has been through the Royal Society of Chemistry peer review process and has been accepted for publication.

*Accepted Manuscripts* are published online shortly after acceptance, before technical editing, formatting and proof reading. Using this free service, authors can make their results available to the community, in citable form, before we publish the edited article. We will replace this *Accepted Manuscript* with the edited and formatted *Advance Article* as soon as it is available.

You can find more information about *Accepted Manuscripts* in the [Information for Authors](#).

Please note that technical editing may introduce minor changes to the text and/or graphics, which may alter content. The journal's standard [Terms & Conditions](#) and the [Ethical guidelines](#) still apply. In no event shall the Royal Society of Chemistry be held responsible for any errors or omissions in this *Accepted Manuscript* or any consequences arising from the use of any information it contains.



Journal Name

ARTICLE

## Highly crystalline, small size, monodisperse $\alpha$ -NiS nanocrystal ink as an efficient counter electrode for dye-sensitized solar cells

Received 00th January 20xx,  
Accepted 00th January 20xx

DOI: 10.1039/x0xx00000x

www.rsc.org/

Xiuwen Wang,<sup>a</sup> Buhe Batter,<sup>a,b</sup> Ying Xie,<sup>a</sup> Kai Pan,<sup>a,\*</sup> Yongping Liao,<sup>a</sup> Chunmei Lv,<sup>a</sup> Mingxia Li,<sup>a</sup> Siyu Sui,<sup>a</sup> and Honggang Fu<sup>a,\*</sup>

We report the synthesis of highly crystalline, small size,  $\alpha$ -NiS nanocrystal inks for the fabrication of counter electrode of dye-sensitized solar cells. The monodisperse  $\alpha$ -NiS nanocrystals (about 7 nm) are obtained via a noninjection, solution-phase chemical synthesis method. During the growth process of  $\alpha$ -NiS nanocrystals, the Ni-oleate complex, which is generated *in situ* from the reaction of nickel chloride and sodium oleate, is decomposed and acts effectively as a growth source in synthesizing monodisperse nanocrystals. By controlling the reaction temperature, the resultant nanocrystal sizes and crystallinity can be well tuned. Compared to conventional obtained NiS bulks, the monodisperse  $\alpha$ -NiS nanocrystals possess an abundance of reaction catalytic sites for dye-sensitized solar cells due to the small particle size and high crystallinity. The first-principles calculations have been first employed to investigate the adsorption energy of  $I_3^-$  molecule on (111) surface of  $\alpha$ -NiS with equilibrium shape. The DSSCs based on monodisperse  $\alpha$ -NiS nanocrystal ink with higher crystallinity display the power conversion efficiency of 7.33 %, which is comparable to that based on Pt cathode (7.53 %), but significantly higher than that based on the bulk NiS (4.64 %) and lower crystallinity  $\alpha$ -NiS nanocrystals (6.32 %). It can be attributed to more reaction catalytic sites due to the surface effect of small  $\alpha$ -NiS nanocrystals, and the highest work function level (5.5 eV) that matched the redox shuttle potential. We believe that our method paves a promising way to design and synthesize advanced counter electrode materials for energy harvesting.

### Introduction

Dye-sensitized solar cells (DSSCs) have attracted extensive attentions during the past quarter century, due to their low cost and high power conversion efficiency (PCE).<sup>1-5</sup> Typically, standard DSSCs consist of three main parts: a dye-sensitized TiO<sub>2</sub> photoanode, a redox electrolyte traditionally containing an iodide/triiodide ( $I^-/I_3^-$ ) couple, and a counter electrode (CE). As an important component of DSSCs, CE collects electrons from external circuit and reduces  $I_3^-$  into  $I^-$ .<sup>6-7</sup> Generally, platinum is considered to be the best counter electrode material and widely used currently. Unfortunately, Pt is relatively scarce and expensive, which forms a large obstacle for scale-up application of DSSC devices. Therefore, lower-cost alternatives for Pt CE in DSSCs need to be urgently sought.

Recently, an extensive effort has been made to develop high-

efficiency and low-cost Pt-free CE materials. Among them, transition metal nitrides<sup>8-9</sup>, carbides<sup>10-11</sup> and sulfides<sup>12-15</sup> have been researched as CE materials due to both their preferentially electrocatalytic activity and facile synthesis. In this respect, nickel sulfide<sup>16-19</sup> is one of the most efficient candidates for their high conductivity and excellent electrocatalytic activity. Small size of nickel sulfide can provide more catalytic sites, and high crystallinity can ensure fast charge transfer. These factors determine the CE properties of DSSCs. Different morphologies of NiS have been fabricated as CE. Wei *et al.* fabricated high-crystalline NiS nanosheet CEs via a one-step hydrothermal route and got high efficiency, which is compared to that of Pt-based DSSCs.<sup>20</sup> Our group previously *in situ* synthesized of a NiS/Ni<sub>3</sub>S<sub>2</sub> nanorod composite array on Ni foil as a FTO-free counter electrode for DSSCs, and it displayed a comparable PCE with Pt-based DSSCs.<sup>21</sup> Chen *et al.* used NiS hollow spheres as the CE of DSSCs.<sup>22</sup> Kim *et al.* prepared high-crystalline nickel sulfide nanoparticles with the size of ca. 40 nm, and it exhibited higher electrocatalytic activity due to the increase of catalytic sites.<sup>23</sup> Also, Meng *et al.* synthesized NiS nanoparticles and nanosheets as CE materials, respectively. Although NiS nanoparticle size is large (ca. 40 nm) and aggregated severely due to its electrochemical synthesis method, DSSCs based on NiS nanoparticles got higher PCE than DSSCs based on NiS

<sup>a</sup>Key Laboratory of Functional Inorganic Material Chemistry, Ministry of Education, Heilongjiang University, Harbin 150080, People's Republic of China. E-mail: kaipan@hlju.edu.cn, fuhg@vip.sina.com. Fax: +86 451 8667 3647; Tel.: +86 451 86604330.

<sup>b</sup>College of Materials and Chemical Engineering, Heilongjiang Institute of Technology, Harbin 150050, People's Republic of China

†Electronic Supplementary Information (ESI) available: See DOI: 10.1039/x0xx00000x

nanosheets.<sup>24</sup> But it is difficult to synthesize the NiS nanocrystals with further decreased size (< 10 nm) because the conventional synthesis methods lack enough tactics to prevent the particle size growth. So, synthesis of NiS nanocrystals with smaller size may be a challenge for further improving the PCE of DSSCs.

In this work, the monodisperse  $\alpha$ -NiS nanocrystals with small size of ca. 7 nm have been controllably synthesized via a noninjection, solution-phase chemical routine based on the Schlenk line system. Compared with previous reports<sup>20-24</sup>, there are two advantages in this work. First, the prepared NiS nanocrystals with small size and high crystallinity possess higher catalytic properties in theory. Second, we provide a tactic to control the growth of small size NiS nanocrystal. During the growth process of  $\alpha$ -NiS nanocrystals, the Ni-oleate complex, which is generated in situ from the reaction of nickel chloride and sodium oleate, is decomposed and acts effectively as a growth source in synthesizing monodisperse nanocrystals. The existence of long-chain ligand reagent (1-octadecene, oleic acid) could encapsulate the NiS nanocrystals effectively and confined the further growth. Moreover, by controlling the reaction temperature, highly crystalline  $\alpha$ -NiS nanocrystals can be obtained. The first-principles calculations have been first employed to investigate the adsorption energy of  $I_3^-$  molecule on (111) surface of  $\alpha$ -NiS with equilibrium shape. The DSSCs based on higher crystalline  $\alpha$ -NiS nanocrystal ink CEs exhibit a PCE of 7.33 %, which was much higher than that of DSSCs based on relatively lower crystalline  $\alpha$ -NiS nanocrystal CEs (6.32 %), and comparable to that of Pt-based DSSCs (7.53 %). Cyclic voltammetry (CV), electrochemical impedance spectroscopy (EIS), and Tafel polarization measurements revealed their excellent electrocatalytic activities towards the  $I_3^-/I^-$  redox reaction. The scanning Kelvin probe (SKP) image indicates the work function of higher crystalline  $\alpha$ -NiS is the highest among Pt-free materials. And it is comparable to that of Pt, which matched the redox shuttle potential. It has been revealed that high crystalline, small size, monodisperse  $\alpha$ -NiS nanocrystals are promising candidates as environment-benign and low-cost Pt-free CE materials for DSSCs.

## Experimental

### Chemicals

Nickel chloride, sulfur power, 1-octadecene (ODE), oleic acid (OA), oleylamine (OLA), ethanedithiol (EDT), ethanol, acetonitrile, hexamethylene and sodium oleate were purchased from standard source. Fluorine doped SnO<sub>2</sub> glass (FTO) (15  $\Omega$ /square, Nippon sheet glass, Japan) was used as electrode substrate. The used Ru complex dye was cis-bis(isothiocyanato)bis(2,2'-bipyridyl-4,4'-dicarboxylato) ruthenium (II) bis-tetrabutylammonium (N719, Solaronix SA, Switzerland). The redox shuttle electrolyte was a blend of 0.1 M LiI (anhydrous, 99 %, Acros), 0.05 M I<sub>2</sub> (anhydrous, 99.8 %), 0.5 M tert-butylpyridine (99 %, Aldrich), 0.1 M guanidine thiocyanate (99 %, Aladdin Co.) and 0.6 M 1-propyl-2, 3-dimethylimidazolium iodide (99 %) in methoxyacetonitrile (99 %, Fluka). All chemicals were used as received without any further purification.

### First-principles calculations of $I_3^-$ adsorption of on NiS surface

The calculations were performed by means of CASTEP package in the density functional theory (DFT) framework.<sup>25</sup> The Perdew-Wang local density approximation form (LAD-PWC) of the exchange correlation energy has been used.<sup>26</sup> During the calculations, the plane-wave and pseudopotential techniques were used, and the energy cutoff was set to 300 eV. To obtain a good numerical sampling of electron densities in Brillouin zone, a (2 $\times$ 2 $\times$ 1) Monkhorst-Pack mesh was applied.<sup>27</sup> For the geometry optimization, a Broyden-Fletcher-Goldfarb-Shanno (BFGS) algorithm was used,<sup>28</sup> and the optimization procedure was repeated until the force, the stress, and the displacement on each atom were less than 0.05 eV $\cdot$  $\text{\AA}^{-1}$ , 0.1GPa, 0.002  $\text{\AA}$ , respectively. This set of parameters also ensured that the total energy of system can be accurately evaluated, and the energy convergences of systems are within 2.0 $\times$ 10<sup>-5</sup> eV $\cdot$ atom<sup>-1</sup>. To determine the stable surfaces of  $\alpha$ -NiS nanocrystals, we have firstly calculated the surface energies by taking the energy difference between the relaxed slabs and the bulk structure with the same amount (n) of  $\alpha$ -NiS formula units as the slab, divided by the surface area of the slab, which can be expressed using the following eqn (1):

$$\gamma = \frac{E_s - nE_a}{2S} \quad (1)$$

where  $E_s$  is the total energy of the slab,  $E_a$  is the total energy of bulk NiS per formula unit, and  $S$  is the surface area of the slab. A vacuum layer of 20  $\text{\AA}$  is adopted for all the calculations, which has been proven enough to remove any spurious interaction between the repeated slabs in the normal direction of the surface.

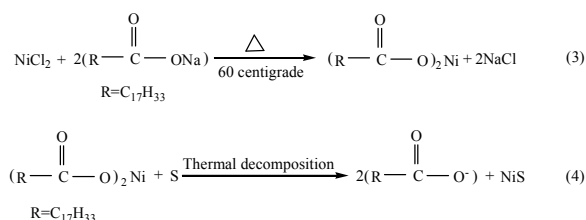
Based on the surface energy calculations, the equilibrium shape of  $\alpha$ -NiS nanocrystals was first obtained thorough the Wulff construction.<sup>29</sup> Then, the adsorption energy between  $I_3^-$  molecule and  $\alpha$ -NiS surface with equilibrium shape has been investigated in order to explain the electrocatalytic activity of the  $\alpha$ -NiS counter electrode in DSSCs. The absorption energies ( $E_b$ ) are defined as eqn (2)

$$E_b = E_{I_3^- - NiS} - (E_{NiS} + E_{I_3^-}) \quad (2)$$

where  $E_{I_3^- - NiS}$  represents the total energy of the  $I_3^-$  and  $\alpha$ -NiS surface with equilibrium shape interacting with each other, is  $E_{NiS}$  the total energy of the  $\alpha$ -NiS surface with equilibrium shape, and  $E_{I_3^-}$  is the total energy of the isolated  $I_3^-$  molecule.

### The synthesis of monodisperse nickel sulfide nanocrystals

The monodisperse nickel sulfide nanocrystals with small size have been controlled fabricated with a noninjection, solution-



phase chemical synthesis based on the Schlenk line. The overall synthetic procedure is depicted in eqn (3) and (4), and the detailed preparation process is as follows. First, the homogeneous reaction solution has been obtained. In details, 0.30 g of sulfur powder was heated into 60 °C to be dissolved in 10.0 mL of OLA by vigorous stirring. Nickel chloride (1.00 g), sodium oleate (3.50 g), distilled water (10.0 mL), ethanol (10.0 mL), hexamethylene (20.0 mL) were then added to the above reaction mixture to obtain the precursor nickel oleate and dissolved sulfur. At last, the 30.0 mL ODE and 1.0 mL OA were added in the reaction system in order to tune the whole solution polarity and boiling limit. Second, the reaction solution was heated at 150 °C for 30 min under the protection of nitrogen flow with intensely stirring to remove impurities and water because of their lower boiling points, and then the reaction temperature rose into 300 °C for 1 h to obtain the monodisperse  $\alpha$ -NiS nanocrystals. Finally, the obtained samples were thoroughly purified by multiple precipitation and redispersion using ethanol and hexamethylene. As a control,  $\alpha$ -NiS nanocrystals with different crystallinity have also been obtained just by adjusting the reaction temperature as 250 and 320 °C. The NiS samples obtained at different reaction temperature X (X = 250, 300, 320) are denoted as NiS-X. Also, the NiS nanoparticles with big size are obtained according to the literature.<sup>30</sup> For large-scale production of  $\alpha$ -NiS nanocrystals, all of the reactants were scaled up to several times than the above recipe with flask.

#### Fabrication of $\alpha$ -NiS CEs and assembly of DSSCs

A thin layer of  $\alpha$ -NiS nanocrystal ink was deposited onto the FTO substrate by spraying coating method, and then the CEs were heated at 400 °C for 30 min under nitrogen atmosphere. Due to the heat treatment, the NiS nanocrystals is somewhat aggregated (Figure S1a). Kim *et al.* also reported the similar phenomenon.<sup>23</sup> The thickness of the film is about 6.0  $\mu\text{m}$  (Figure S1b). The CEs fabricated with NiS-X (X = 250, 300, 320) and bulk-NiS were labeled as  $E_{\text{NiS-250}}$ ,  $E_{\text{NiS-300}}$ ,  $E_{\text{NiS-320}}$ , and  $E_{\text{bulk-NiS}}$ , respectively. As a control, a mirror-like Pt CEs ( $E_{\text{Pt}}$ ) were prepared according to the standard routine.<sup>31-32</sup>

The dye-sensitized  $\text{TiO}_2$  photoanodes were prepared according to the conventional method.<sup>33-34</sup> The dye-sensitized  $\text{TiO}_2$  photoanode was assembled with a CE into a sandwich-type cell. After the injection of redox electrolyte, the sandwich-type cell was further sealed with a thermoplastic hot-melt Surlyn (30  $\mu\text{m}$ ). The fabricated DSSCs based on cathodes of  $E_{\text{NiS-250}}$ ,  $E_{\text{NiS-300}}$ ,  $E_{\text{NiS-320}}$ ,  $E_{\text{bulk-NiS}}$  and  $E_{\text{Pt}}$  were labeled as  $C_{\text{NiS-250}}$ ,  $C_{\text{NiS-300}}$ ,  $C_{\text{NiS-320}}$ ,  $C_{\text{bulk-NiS}}$  and  $C_{\text{Pt}}$ , respectively. And the dummy cells with two identical  $E_{\text{NiS-250}}$ ,  $E_{\text{NiS-300}}$ ,  $E_{\text{NiS-320}}$  and  $E_{\text{Pt}}$  were fabricated for EIS and Tafel polarization measurement. They were labeled as  $\text{DC}_{\text{NiS-250}}$ ,  $\text{DC}_{\text{NiS-300}}$ ,  $\text{DC}_{\text{NiS-320}}$  and  $\text{DC}_{\text{Pt}}$ , respectively.

#### Characterizations

The composition of the materials was studied by X-ray diffraction (XRD), which were recorded using a Rigaku D/max-IIIB diffractometer with  $\text{Cu K}\alpha$  ( $\lambda = 1.5406 \text{ \AA}$ ). X-ray photoelectron spectroscopy (XPS) analysis was performed on a

VG ESCALAB MK II with an Mg Ka (1253.6 eV) achromatic X-ray source. Transmission electron microscopy (TEM) experiment was performed on a JEM-3010 electron microscope (JEOL, Japan) with an acceleration voltage of 200 kV. Scanning electron microscopy (SEM) images were taken using a Hitachi S-4800 instrument operating at 15 kV. The particle size was measured by dynamic light scattering method with a SZ-100 nanometer particle / Zeta potential analyzer (SZ-100, Japan). The scanning Kelvin probe (SKP) measurements (SKP5050 system, Scotland) have been performed at normal conditions of laboratory (in ambient atmosphere). A gold electrode was used as the reference electrode and the air gap between probe and sample was kept at 70  $\mu\text{m}$ . The vibration of the tip electrode was 50  $\mu\text{m}$ .

Photovoltaic measurements were carried out with a solar simulator (Oriel, USA) equipped with an AM 1.5G filter (Oriel, USA). The power of the simulated light was calibrated to 100  $\text{mWcm}^{-2}$  by using an Oriel solar simulator radiometer. Current-voltage ( $J$ - $V$ ) curves were measured with a BAS100B electrochemical analyzer (Zahner Elektrik, Germany). The area of DSSCs is 1.5  $\text{cm}^2$ , and the irradiation area is 0.12  $\text{cm}^2$  with a photomask. The NiS films were made in the same batch. Each value for cell performance was determined as an average of at least 3 samples. The EIS were performed in a dummy cell with a computer-controlled IM6e impedance measurement unit (Zahner Elektrik, Germany) and carried out by applying sinusoidal perturbations of 10 mV, and the frequency ranges from 10 mHz to 1 MHz. The obtained spectra were fitted with ZsimpWin software in terms of appropriate equivalent circuits. The Tafel polarization measurements were carried out with BAS100B electrochemical analyzer in a dummy cell. The CV curves were carried out in a three-electrode system in a nitrogen-purged acetonitrile solution, which contains 0.1 M  $\text{LiClO}_4$ , 10 mM LiI and 1 mM  $\text{I}_2$ , at a scan rate of 25  $\text{mV s}^{-1}$ . Thereinto, the Pt worked as an auxiliary electrode, versus the  $\text{Ag}/\text{Ag}^+$  reference electrode.

## Results and discussion

### Adsorption of $\text{I}_3^-$ on the surface of $\alpha$ -NiS with equilibrium shape

**Table 1** Surface energies of  $\alpha$ -NiS in eight orientations that appear in the Wulff shape of  $\alpha$ -NiS.

Orientation	(001)	(010)	(101)	(110)
$\gamma$ ( $\text{J m}^{-2}$ )	1.08	1.24	0.57	0.64
Orientation	(111)	(210)	(201)	(102)
$\gamma$ ( $\text{J m}^{-2}$ )	0.53	0.87	0.65	0.85

According to the eqn (1), the calculated surface energies for eight surfaces of  $\alpha$ -NiS are listed in Table 1. Among these investigated orientations, (111) surface presents the lowest energy (0.53  $\text{J m}^{-2}$ ). The surface energies of all orientations increase in the order of (111) < (101) < (110) < (201) < (102) < (210) < (001) < (010). Based on the surface energy calculations,

the equilibrium shape of  $\alpha$ -NiS nanocrystals was obtained through the Wulff construction (Figure 1a). In general, the lower in energy a surface is, the more area it contributes to the Wulff shape. The (111) and (101) surfaces with relatively low surface energies in the equilibrium shape contribute up to the most surface area. Therefore, the surface properties of  $\alpha$ -NiS nanocrystals are mainly controlled by surfaces (111) and (101) surface.

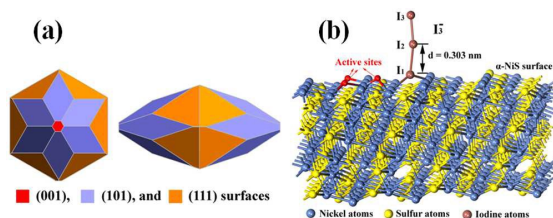


**Figure 1** (a) Top view and side view of the Wulff construction of  $\alpha$ -NiS nanocrystals based on the calculated surface energies in various directions; (b) 3D view of  $I_3^-$  complex absorption on  $\alpha$ -NiS surface with the equilibrium shape.

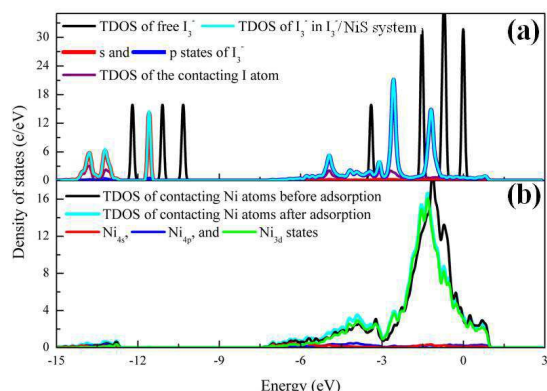


**Figure 2** Density of states (DOSs) for (a)  $I_3^-$  molecule and (b) Ni atoms in the  $I_3^-/\alpha$ -NiS systems.

To determine the energetically preferred adsorption, the  $I_3^-$  complex was placed initially on the most stable (111) surface, and after geometry optimization, the converged structures were obtained (Figure 1b). The calculated adsorption energies of  $I_3^-$  on the  $\alpha$ -NiS surfaces were  $-1.83$  eV. The result indicated that when  $I_3^-$  adsorbed on  $\alpha$ -NiS surface, the adsorption energy decreased significantly, which suggest that the interaction between  $I_3^-$  and  $\alpha$ -NiS surface is strong. The original bond length of  $I_1-I_2$  in the free  $I_3^-$  complex was  $0.298$  nm and increase to  $0.303$  nm as it was attached to the  $\alpha$ -NiS surface. Due to the strong interaction between  $I_1$  and  $\alpha$ -NiS surface, the electron clouds of  $I_1$  atom adsorbed on the  $\alpha$ -NiS surface shift away from the near  $I_2$  atom, the interaction between  $I_1$  and  $I_2$  atom decreased. So,  $I_1-I_2$  bond length is increased. The longer the  $I_1-I_2$  bond, the more activated the  $I_3^-$  is.<sup>14</sup> So, the  $\alpha$ -NiS has an excellent catalytic activity for  $I_3^-$ .

To further reveal the interactions between  $I_3^-$  and  $\alpha$ -NiS, the total and partial density of states (PDOSs) were calculated (Figure 2). In all calculations, the Fermi energy was taken as zero point ( $E-E_f = 0$  eV). After  $I_3^-$  is adsorbed on  $\alpha$ -NiS surface, the DOSs of  $\alpha$ -NiS and  $I_3^-$  system are changed significantly. It is found that the 5p states of I atom are changed obviously and

shifted to lower energy position, while the DOSs of the contacting metal atoms also varied significantly. According to the partial density of states, it can be further identified that the changed states are mainly originated from Ni3d states. Therefore, the interactions between I5p and Ni3d states can be confirmed. So, the  $\alpha$ -NiS nanocrystals are efficient for the regeneration of  $I_3^-/I^-$  redox couples in DSSCs. The  $\alpha$ -NiS nanocrystal ink as a counter electrodes maybe obtain a satisfying PCE in DSSCs.

### Structural characterization of $\alpha$ -NiS nanocrystals

The  $\alpha$ -NiS nanocrystals with small size have been controllably synthesized following above described reaction process. During the growth process of  $\alpha$ -NiS nanocrystals, the Ni-oleate complex, which is generated in situ from the reaction of nickel chloride and sodium oleate, is decomposed and acts effectively as a nickel source, reacting with dissolved sulfur, resulting in synthesis of monodisperse  $\alpha$ -NiS nanocrystals.<sup>35</sup> XRD measurements were carried out to characterize the crystallinity and structure of the NiS nanocrystals (Figure 3). The diffraction peaks at  $30.19^\circ$ ,  $34.88^\circ$ ,  $46.07^\circ$ ,  $53.67^\circ$  and  $73.33^\circ$  can be observed for NiS-250 and NiS-300, which is assigned to the (100), (101), (102), (110) and (202) planes of hexagonal phase of NiS ( $\alpha$ -NiS, P63/mmc) (JCPDS, PDF No. 02-1280). The Full Width and Half Maximum (FWHM) values with different planes of NiS-250 and NiS-300 samples are calculated and listed in the Table S1. It can be seen that the FWHM value of NiS-300 is smaller than that of NiS-250, therefore the NiS-300 had has a relatively higher crystallinity.<sup>36</sup> The Scherrer formula was used to calculate the nanocrystal size of NiS-300 using (101) plane (Figure S2), the calculated nanocrystal size is ca. 13 nm. When the temperature rose to  $320^\circ\text{C}$ , there appears the rhombohedral phase of NiS ( $\beta$ -NiS, JCPDS, PDF No.12-0041) and a small amount of  $Ni_9S_8$  (JCPDS, PDF No.22-1193), besides  $\alpha$ -NiS.

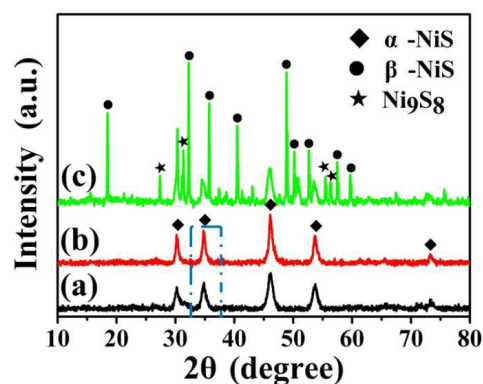


**Figure 3** X-ray diffraction patterns of NiS-250 (a), NiS-300 (b) and NiS-320 (c).

The high-resolution XPS spectra of Ni2p and S2p were measured to determine the oxidation states of the  $\alpha$ -NiS constituent elements (Figure 4). The binding energies of the Ni 2p<sub>3/2</sub> peaks are  $855.4$  eV for NiS-300 (Figure 4a), which indicated that the oxidation state of Ni was +2. The binding energies of the S 2p<sub>1/2</sub> and S 2p<sub>3/2</sub> peaks are  $162.4$  and  $161.4$  eV, indicating that most of the S species exist as  $S^{2-}$  (Figure 4b).<sup>24</sup> The result is close to the previous reported values for

NiS.<sup>37-38</sup> Therefore, a hexagonal  $\alpha$ -NiS phase was obtained via a noninjection, wet solution-phase chemical synthesis based on the Schlenk line. Moreover, the XPS spectra were also measured to determine the oxidation states of the NiS-250 and NiS-320 (Figure S3). The binding energies of the Ni 2p<sub>3/2</sub>, S 2p<sub>1/2</sub> and S 2p<sub>3/2</sub> peaks for NiS-250 are same to that for NiS-300, which indicated that the Ni and S species exist as Ni<sup>2+</sup> and S<sup>2-</sup>. But for the NiS-320, the binding energies of the Ni 2p<sub>3/2</sub> peaks are 855.0 eV, which is less than that of NiS. That is because of the existence of Ni<sub>9</sub>S<sub>8</sub>. The binding energies of the S 2p<sub>1/2</sub> and S 2p<sub>3/2</sub> peaks have no change. The XPS data are consistent with the XRD data.

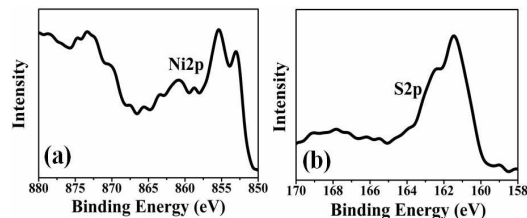


**Figure 4** XPS of NiS-300 for Ni 2p region (a) and S 2p region (b), respectively.

TEM image shows that the fabricated NiS-300 is monodisperse nanocrystals with a small size of *ca.* 7 nm (Figure 5a, d). The particle size of NiS is detected by dynamic light scattering measurements and it had been added as Figure S4 in the revised manuscript. The result shows that the prepared NiS-300 is monodisperse nanocrystals with a small size of *ca.* 7.7 nm. The dynamic light scattering measurements results agree with the TEM results. It further confirmed that NiS-300 nanocrystals with small size of *ca.* 7 nm have been controllably synthesized. The Scherrer formula was also used to calculate the nanocrystal size of NiS-300 using (101) plane (Figure S2). And the calculated nanocrystal size is *ca.* 13 nm. The NiS nanocrystals have been dried before the XRD measurement, which results in the aggregation of nanocrystals. So, the size deviation formed between the calculated data based on the XRD and the measured data based on the TEM image and dynamic light scattering. The lattice spacing of 0.29, 0.19 and 0.26 nm could be clearly observed in HRTEM image (Figure 5b), which corresponded to the (100), (102) and (101) planes of  $\alpha$ -NiS, respectively. And the HRTEM image showed distinct lattice fringe patterns, indicating the highly crystalline nature of the nanocrystals. The selected area electron diffraction (SAED) pattern also verified that  $\alpha$ -NiS was polycrystalline (Figure 5c). It could be seen that NiS-250 and NiS-300 have the same diffraction ring spacing, which corresponded the same (100) plane of  $\alpha$  phase NiS (Figure S5a and Figure 5c). The spots in the diffraction ring of NiS-300 are brighter than that of NiS-250, which means that the NiS-300 has better crystallinity than NiS-250 to some extent. The diffraction ring spacing of NiS-320 has changed, which corresponded the (110) plane of  $\beta$  phase NiS (Figure S5b). Because the rise of reaction temperature results in the highest crystallinity, the spots in the diffraction ring of NiS-320 are brightest.

The TEM images of NiS-250 and NiS-320 nanocrystals were also showed in Figure S6. As the reaction temperature rises into 320 °C, the  $\alpha$ -NiS nanocrystals become bigger and polydisperse. The interplanar spacings of 0.24 nm and 0.25 nm could be observed in the HRTEM image of NiS-320, which corresponds to the (220), (021) of  $\beta$ -NiS, respectively. It further confirmed that NiS-320 have  $\beta$  phase, besides  $\alpha$ -NiS. The obtained bulk NiS particle is about 200 nm. The EDS indicates the formation of NiS (Figure S7). All the measurement indicated that the monodisperse  $\alpha$ -NiS nanocrystals with small size and high crystallinity were synthesized.

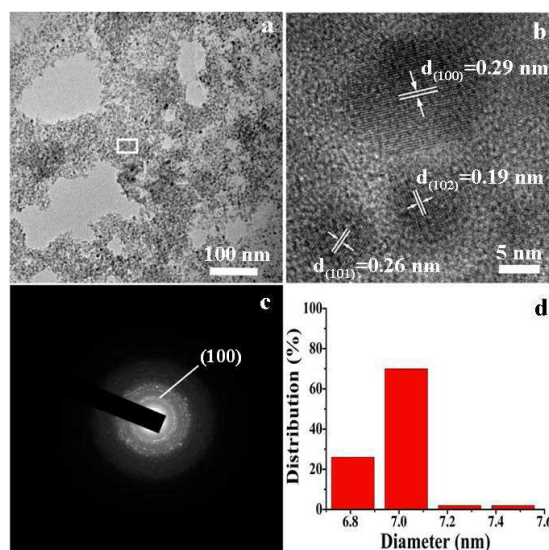


**Figure 5** (a) TEM, (b) HRTEM and (c) SAED images of the NiS-300, (d) The corresponding particle size distribution of  $\alpha$ -NiS nanocrystals in image (a).

#### Photoelectrical character of DSSCs

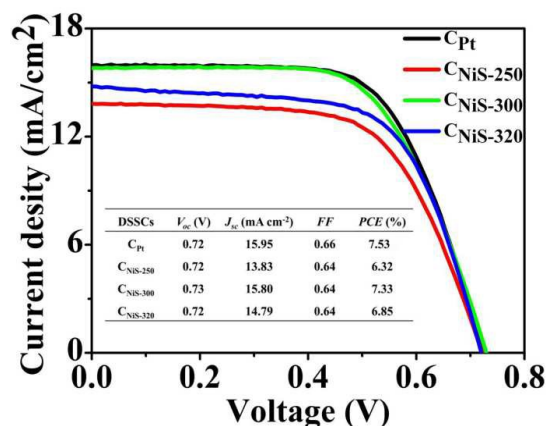


**Figure 6** Typical current-voltage curves of DSSCs based on Pt (C<sub>Pt</sub>) and NiS (C<sub>NiS-250</sub>, C<sub>NiS-300</sub>, C<sub>NiS-320</sub>) CEs under one sun illumination (AM 1.5G).

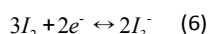
The prepared  $\alpha$ -NiS was used as the counter electrode to obtain high-efficiency DSSCs. The NiS nanocrystals were typically passivated with *ca.* 2.5 nm long alkyl ligands (OA and OLA), which was harmful to the charge transfer due to the ligand preventing close  $\alpha$ -NiS nanocrystals packing. The  $\alpha$ -NiS

film counter electrodes were subsequently dipped in 15 mM EDT in an acetonitrile solution for 20 s to remove the long chain ligands from the  $\alpha$ -NiS surfaces and to reduce the interparticle spaces of nanocrystals. The  $J$ - $V$  curves of DSSCs are shown in Figure 6. The photovoltaic parameters of the DSSCs, including open-circuit voltage ( $V_{oc}$ ), short-circuit current density ( $J_{sc}$ ), fill factor (FF), and PCE are listed in Table inset in Figure 6. The PCE of  $C_{NiS-300}$  reaches 7.33 %, which is better than that of  $C_{NiS-250}$  (6.32 %),  $C_{NiS-320}$  (6.85 %) and  $C_{bulk-NiS}$  (4.64 %) (Figure S8). It shows the best performance among Pt-free counter electrodes, and is comparable to that of Pt-based DSSCs (7.53%).  $C_{NiS-250}$  shows comparatively poor cell performance due to lower crystallinity of NiS-250. Although the crystallinity of NiS-320 further improved, the  $J_{sc}$ ,  $V_{oc}$  and PCE of  $C_{NiS-320}$  decrease compared with  $C_{NiS-300}$ . It may be attributed to the increased interface charge transfer resistance owing to the presence of  $\beta$ -NiS and a small amount of  $Ni_9S_8$  in NiS-320. The  $C_{bulk-NiS}$  possessing the lowest PCE is due to fewer active sites exposing in the NiS surface.

### The key factors determining the photoelectrical properties

It is known that the performance of DSSCs is strongly dependent on the electrocatalytic activity and interface charge transfer of CEs while retaining other cell components identical.<sup>39-40</sup> In the following, the CV, EIS and Tafel methods are used to study the catalytic activity and electron transfer of the as-prepared CEs in detail.

To understand the electrocatalytic activity of the counter electrodes, CV of various CEs has been carried out (Figure 7a). Two typical pairs of redox peaks are observed in all cases, which represented sequential redox reactions of different iodide species, as shown in the below eqn (5) and (6)



The electrochemical reduction of  $I_3^-$  in the low potential range is the regeneration of the redox species on the CE of DSSCs. As shown in Figure 7a, two pairs of redox peaks are observed for  $E_{NiS-250}$ ,  $E_{NiS-300}$  and  $E_{NiS-320}$  cathodes, which are similar to those of Pt cathodes. It is implied that the three Pt-free cathodes operate through a similar catalytic mechanism Pt cathodes. Remarkably, the cathodic current density of the  $E_{NiS-300}$  is the highest among the three Pt-free cathodes, comparable to that of the Pt cathode, suggesting that the  $E_{NiS-300}$  has better electrocatalytic activity. Figure 7a clearly shows that NiS-300 has the best catalytic activities among the Pt-free nanomaterials, and the DSSCs based on the NiS-300 cathode possess the best PCE among the Pt-free based DSSCs, which agrees with the  $J$ - $V$  results.

Figure 7b shows the consecutive CV curves of the NiS-300 cathode. It can be seen that NiS-300 cathode have the similar work stability with the Pt cathode (Figure S9). No obvious current density decline and peak shifts are observed after a 20-cycle test. It indicates that the NiS-300 cathode has excellent electrochemical stability in the  $I^-/I_3^-$  electrolyte solution.

Tafel polarization measurement is used to further investigate the catalytic activities of the CEs. Typically, the Tafel curve can be separated into three zones: polarization zone (low potential), Tafel zone (intermediate potential with a sharp slope), and diffusion zone (high potential). The information about the exchange current density ( $J_0$ ) can be obtained from the Tafel zone.<sup>41</sup> The Tafel polarization curves measured with symmetrical dummy cell are shown in Figure 7c. In the Tafel zone, the tangent slope of the curve provides information about  $J_0$ , which is closely related to charge transfer resistance ( $R_{ct}$ ) value according to eqn (7).

$$J_0 = \frac{RT}{nFR_{ct}} \quad (7)$$

Where  $R$  is the gas constant,  $T$  is the temperature,  $F$  is the Faraday constant, and  $n$  is the total number of individuals.

The  $DC_{NiS-300}$  exhibited a larger  $J_0$  in comparison with that of  $DC_{NiS-320}$  and  $DC_{NiS-250}$ , indicating the superior catalytic activity for  $DC_{NiS-300}$  among the three Pt-free CEs and the superior catalytic activity of NiS-300.

EIS represents the intrinsic interfacial charge transfer and charge transport kinetics at the electrode/electrolyte interface. The Nyquist plots of dummy cells ( $DC_{NiS-250}$ ,  $DC_{NiS-300}$ ,  $DC_{NiS-320}$ , and  $DC_{Pt}$ ) are shown in Figure 7d. In the plot, two semicircles were clearly observed, which were obtained by changing the frequency from 10 mHz to 1 MHz. The high frequency intercept on the real axis represents the series resistance ( $R_s$ ). The left semicircle in the middle frequency can be attributed to the charge transfer resistance ( $R_{ct}$ ). Additionally, the right semicircle in the low frequency range reflects the Nernst diffusion impedance ( $Z_N$ ) of the redox couple transport in the electrolyte. Figure S10 shows the equivalent circuit, which used to fit the experimental EIS data. It can be seen that  $R_{ct}$  is

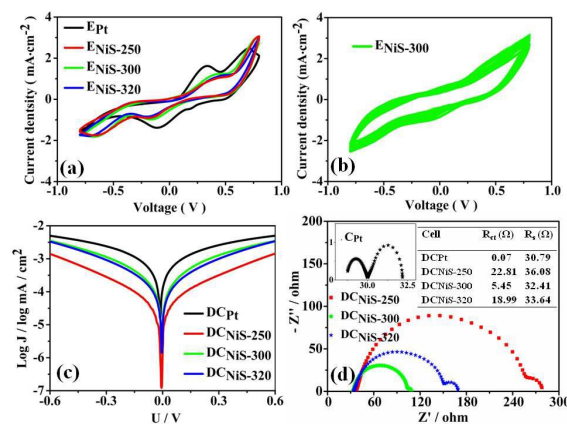


**Figure 7** (a) CV spectra for the series of cathodes at a scan rate of  $25 \text{ mV s}^{-1}$ . (b) Twenty consecutive CV spectra for the  $E_{NiS-300}$  at a scan rate of  $25 \text{ mV s}^{-1}$ . (c) Tafel polarization curves for the symmetrical cells ( $DC_{Pt}$ ,  $DC_{NiS-250}$ ,  $DC_{NiS-300}$  and  $DC_{NiS-320}$ ). (d) EIS Nyquist plots of dummy cells fabricated in the same way as the ones used in the Tafel experiments. Inset in (d) left is a Nyquist plot of  $DC_{Pt}$  and right is detail parameters of dummy cells, respectively.

5.45  $\Omega$  for DC<sub>NiS-300</sub>, 18.99  $\Omega$  for DC<sub>NiS-320</sub>, 22.81  $\Omega$  for DC<sub>NiS-250</sub>. This result demonstrates that the E<sub>NiS-300</sub> possess faster interfacial charge transfer than E<sub>NiS-250</sub> and E<sub>NiS-320</sub>. The values of R<sub>s</sub> for the DSSCs with DC<sub>NiS-250</sub>, DC<sub>NiS-300</sub>, DC<sub>NiS-320</sub>, and DC<sub>Pt</sub> are 36.08, 32.41, 33.64, and 30.79  $\Omega$ , respectively, which indicate that the adhesion property between  $\alpha$ -NiS nanocrystal ink and FTO substrate is comparable to Pt. As well known, the series and shunt resistances are the solo factor to determine the fill factors.<sup>42</sup> In this work, the series resistances are relatively high, which results in the lower fill factor. It agrees with the J-V results.

Taking the above results into consideration, including CV, EIS and Tafel polarization, the CE based on monodisperse  $\alpha$ -NiS nanocrystals with higher crystallinity and small size (NiS-300) displays the highest catalytic activity towards the reducing of I<sub>3</sub><sup>-</sup> and fastest charge transfer among the Pt-free CEs. It is also comparable to Pt CE.

#### The possible catalytic mechanism for redox shuttle

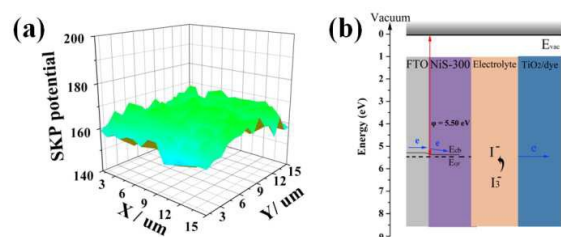


**Figure 8** Work function map (a) and the energy level of NiS-300 electrode (b).

The surface area and crystallinity of  $\alpha$ -NiS nanocrystals could affect the DSSC performance significantly. Large surface area and high crystallinity could provide more electrocatalytic sites and faster electron transfer. The monodisperse NiS-300 with size of 7 nm possess large surface area, so it provides more electrocatalytic activity sites for the reduction of redox shuttle. Moreover, in order to further identify that the monodisperse NiS-300 with high crystallinity is more beneficial for the electron transfer than NiS-250 and NiS-320, the SKP measurement was taken. The SKP is an awfully sensitive instrument capable of discerning subtle molecular interactions using vibrating electromagnetic fields. Electrode based on NiS-300 (E<sub>NiS-300</sub>) shows a relative flat Fermi level, and the work-function ( $\phi$ ) value is 5.50 eV (Figure 8a). It is the highest value among the Pt-free electrodes (5.45 eV for E<sub>NiS-250</sub>, 5.47 eV for E<sub>NiS-320</sub>; Figure S11 (a, b)), which also is very closed to that of Pt (5.65 eV). The work function difference affected the barrier height at the NiS/FTO interface. The built-in field and the depletion layer width depend on the doping density. High crystalline materials may have lower recombination rate and/or high conductivity. The increased  $\phi$  results in the increased built-in field. So the increased work function results in the increased built-in field for NiS-300, which favor the fast photoelectron transfer across the NiS/FTO interface. So, the NiS-300 is more favorable for the electron transfer than NiS-250 and NiS-320 (Figure 8b). Therefore, DSSCs based on NiS-300 CE get

improved photocurrent density among Pt-free CE. And they get high PCE that is comparable to that of Pt CE.

#### Conclusions

In summary, the monodisperse  $\alpha$ -NiS nanocrystals with small size of 7 nm and high crystallinity have been prepared via a noninjection, solution-phase chemical synthesis method. The first-principles calculation results indicated the bond length of I-I increased from 0.298 nm in the free I<sub>3</sub><sup>-</sup> complex to 0.303 nm as it was attached to the (111) surface of  $\alpha$ -NiS with the equilibrium shape. A PCE of 7.33 % was achieved when the DSSCs are fabricated with monodisperse  $\alpha$ -NiS with higher crystallinity (E<sub>NiS-300</sub>), which is comparable to that of Pt CE. The enhanced performance arises from abundant active sites and fast interface charge transfer of E<sub>NiS-300</sub>. The electrochemical tests can further identify that the E<sub>NiS-300</sub> has high electrocatalytic activity and fast charge transfer for redox shuttle. These results may pave the way for the further study of environmentally friendly, stable, highly efficient counter electrodes for DSSCs.

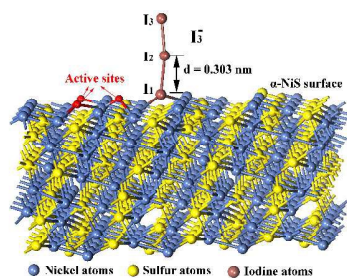
#### Acknowledgements

We gratefully acknowledge the support of this research by the National Natural Science Foundation of China (21473051, 21371053, 21201059), Program for Innovative Research Team in University (IRT-1237).

#### Notes and references

- B. O'Regan and M. Grätzel, *Nature*, 1991, **353**, 737-740.
- M. Grätzel, *Nature*, 2001, **414**, 338-344.
- M. K. Nazeeruddin, S. Fantacci, S. Ito, B. Takeru, G. Viscardi, M. Grätzel, A. Selloni, F. D. Angelis and P. Liska, *J. Am. Chem. Soc.*, 2005, **127**, 16835-16847.
- M. Wang, N. Chthalie, L. Breau, J.-E. Moser, R. H.-Baker, B. Marsan, S. M. Zakeeruddin and M. Grätzel, *Nature Chem.*, 2010, **2**, 385-389.
- J.-Y. Liao, J.-W. He, H. Xu, D.-B. Kuang and C.-Y. Su, *J. Mater. Chem.*, 2012, **22**, 7910-7918.
- Q. Tai, B. Chen, F. Guo, S. Xu, H. Hu, B. Sebo and X. Zhao, *ACS Nano*, 2011, **5**, 3795-3799.
- T. Wang, C. Zhang, X. Sun, Y. Guo, H. Guo, J. Tang, H. Xue, M. Liu, X. Zhang, L. Zhu, Q. Xie and J. Xie, *J. Power Sources*, 2012, **212**, 1-12.
- G. R. Li, J. Song, G. L. Pan and X. P. Gao, *Energy Environ. Sci.*, 2011, **4**, 1680-1683.
- M. Wu, H. Guo, Y.-n. Lin, K. Wu, T. Ma and A. Hagfeldt, *J. Phys. Chem. C*, 2014, **118**, 12625-12631.
- Y. Liao, Y. Xie, K. Pan, G. Wang, Q. Pan, W. Zhou, L. Wang, B. Jiang and H. Fu, *ChemSusChem*, 2015, **8**, 726-733.
- M. Wu, Y. Lin, H. Guo, K. Wu and X. Lin, *Chem. Commun.*, 2014, **57**, 7625-7627.
- C.-W. Kung, H.-W. Chen, C.-Y. Lin, K.-C. Huang, R. Vittal, K.-C. Ho, *ACS Nano*, 2012, **6**, 7016-7025.
- H. K. Mulmudi, S. K. Batabyal, M. Rao, R. R. Prabhakar, N. Mathews, Y. M. Lam and S. G. Mhaisalkar, *Phys. Chem. Chem. Phys.*, 2011, **13**, 19307-19309.

- 14 Y. -C. Wang, D.-Y. Wang, Y.-T. Jiang, H.-A. Chen, C.-C. Chen, K.-C. Ho, H.-L. Chou and C.-W. Chen, *Angew. Chem., Int. Ed.*, 2013, **52**, 6694–6698.
- 15 W. Ke, G. Fang, H. Lei, P. Qin, H. Tao, W. Zeng, J. Wang and X. Zhao, *J. Power Sources*, 2014, **248**, 809–815.
- 16 W. Ke, G. Fang, H. Tao, P. Qin, J. Wang, H. Lei, Q. Liu and X. Zhao, *ACS Appl. Mater. Interfaces*, 2014, **6**, 5525–5530.
- 17 X. Yang, L. Zhou, A. Feng, H. Tang, H. Zhang, Z. Ding, Y. Ma, M. Wu, S. Jin and G. Li, *J. Mater. Res.*, 2014, **29**, 935–941.
- 18 Y. Li, H. Wang, H. Zhang, P. Liu, Y. Wang, W. Fang, H. Yang, Y. Li and H. Zhao, *Chem. Commun.*, 2014, **50**, 5569–5571.
- 19 H.-M. Chuang, C.-T. Li, M.-H. Yeh, C.-P. Lee, R. Vittal and K.-C. Ho, *J. Mater. Chem. A*, 2014, **2**, 5816–5824.
- 20 X. Sun, J. Dou, F. Xie, Y. Li and M. Wei, *Chem Commun.*, 2014, **50**, 9869–9871.
- 21 Y. Liao, K. Pan, Q. Pan, G. Wang, W. Zhou and H. Fu, *Nanoscale*, 2015, **7**, 1623–1626.
- 22 X. Yang, J. Luo, L. Zhou, B. Yang, X. Zuo, G. Li, H. Tang, H. Zhang, M. Wu and Y. Ma, S. Jin, Z. Sun and X. Chen, *Mater. Lett.*, 2014, **136**, 241–244.
- 23 W. Chi, J. Han, S. Yang, D. Roh, H. Lee and H. Kim, *Chem. Commun.*, 2012, **48**, 9501–9503.
- 24 H. Sun, D. Qin, S. Huang, X. Guo, D. Li, Y. Luo and Q. Meng, *Energy Environ. Sci.*, 2011, **4**, 2630–2637.
- 25 Y. Li, J. Zhang, F. Yang, J. Liang, H. Sun, S. Tang and R. Wang, *Phys. Chem. Chem. Phys.*, 2014, **16**, 24604–24609.
- 26 J. P. Perdew, J. A. Chevary, S. H. Vosko, K. A. Jackson, M. R. Pederson, D. J. Singh and C. Fiolhais, *Phys. Rev. B*, 1992, **46**, 6671–6687.
- 27 H. J. Monkhorst and J. D. Pack, *Phys. Rev. B*, 1976, **13**, 5188–5192.
- 28 T. H. Fischer and J. Almlöf, *J. Phys. Chem.*, 1992, **96**, 9768–9774.
- 29 S. Ganapathy and M. Wagemaker, *ACS Nano*, 2012, **6**, 8702–8712.
- 30 J. Wang, S. Y. Chew, D. Wexler, G. X. Wang, S. H. Ng, S. Zhong and H. K. Liu, *Electrochem. Commun.*, 2007, **9**, 1877–1880.
- 31 A. Hagfeldt and M. Grätzel, *Acc. Chem. Res.*, 2000, **33**, 269–277.
- 32 X. Miao, K. Pan, Q. Pan, W. Zhou, L. Wang, Y. Liao, G. Tian and G. Wang, *Electrochim. Acta*, 2013, **96**, 155–163.
- 33 H. Jeong, Y. Pak, Y. Hwang, H. Song, K. Lee, H. Ko and G. Jung, *Small*, 2012, **8**, 3757–3761.
- 34 S. Ito, P. Chen, P. Comte, M. Nazeeruddin, P. Liska, P. Péchy and M. Grätzel, *Prog. Photovoltaics*, 2007, **15**, 603–612.
- 35 J. Park, K. An, Y. Hwang, J. Park, H. Noh, J. Kim, J. Park, N. Hwang and T. Hyeon, *Nature Mater.*, 2004, **3**, 891–895.
- 36 B. Cullity, S. Stock, in *Elements of X-ray Diffraction*, Prentice Hall, 3rd edn., 2001. vol. 1, ch. 6, pp. 173–174.
- 37 S. Yan, Y. Shi, L. Sun, Z. Xiao, B. Sun and X. Xu, *Mater. Sci. Eng., B*, 2013, **178**, 109–116.
- 38 N. Chen, W. Zhang, W. Yu and Y. Qiao, *Mater. Lett.*, 2002, **55**, 230–233.
- 39 M. Wu, X. Lin, Y. Wang, L. Wang, W. Guo, D. Qi, X. Peng, A. Hagfeldt, M. Grätzel and T. Ma, *J. Am. Chem. Soc.*, 2012, **134**, 3419–3428.
- 40 S. Yun, A. Hagfeldt and T. Ma, *Adv. Mater.*, 2014, **26**, 6210–6237.
- 41 M. Wu, X. Lin, A. Hagfeldt and T. Ma, *Angew. Chem., Int. Ed.*, 2011, **123**, 3520–3524.
- 42 Y. Huang, S. Y. Dai, S. H. Chen, C. N. Zhang, Y. F. Sui, S. F. Xiao, L. H. Hu, *App. Phys. Lett.*, 2009, **95**, 243503 (3pp).



The  $\alpha$ -NiS nanocrystals have excellent catalytic activities for  $I_3^-$  reduction for the strong interaction between  $I_1$  and  $\alpha$ -NiS active sites.